Analytica Chimica Acta 1208 (2022) 339825

Contents lists available at ScienceDirect

Analytica Chimica Acta

journal homepage: www.elsevier.com/locate/aca

Ratiometric fluorescence biosensor for imaging of protein phosphorylation levels in atherosclerosis mice

Wei Zhang *, Jin Li, Na Zhao, Ping Li, Wen Zhang, Hui Wang, Bo Tang

College of Chemistry, Chemical Engineering and Materials Science, Collaborative Innovation Center of Functionalized Probes for Chemical Imaging in Universities of Shandong, Key Laboratory of Molecular and Nano Probes, Ministry of Education, Institute of Biomedical Sciences, Shandong Normal University, Jinan, 250014, PR China

HIGHLIGHTS

- Ratiometric fluorescence nanosensor PCN/W–B@BSA was prepared and applied for ratio fluorescence imaging of protein phosphorylation level in the AS mice model.
- Using the two-photon imaging, the background is significantly reduced, and the sensitivity of imaging analysis is improved by combining with ratio imaging.
- This study provides suitable fluorescence tool for further revealing phosphorylation related signaling pathways and disease mechanisms.

GRAPHICAL ABSTRACT

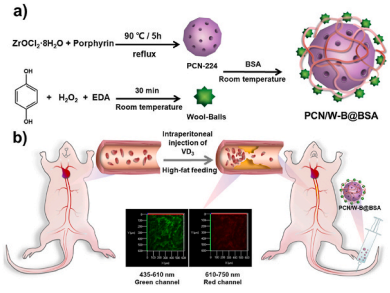

ABSTRACT

Atherosclerosis (AS) is the main cause of coronary heart disease, cerebral infarction and peripheral vascular disease, which is an important disease threatening human health. Abnormal levels of protein phosphorylation are closely related to the occurrence and development of diseases. Herein, the ratiometric fluorescence nanosensor (PCN/W– B@BSA) was prepared by using metal-organic frameworks (PCN-224) and fluorescent nanocluster wool-balls, which was applied for ratiometric fluorescence imaging of protein phosphorylation level in the AS mice model. Specific recognition of phosphorylation sites was achieved *via* specific interaction between active center Zr(IV) and phosphate. Using the two-photon property of porphyrin, the background is significantly reduced, and the sensitivity of imaging analysis is improved by combining with ratio imaging. Bovine serum albumin (BSA) was used to modify the surface of the nanosensor to reduce the non-specific adsorption and improve the biocompatibility of the nanosensor. Finally, the fluorescence nanosensor was successfully apply to fluorescence imaging of protein phosphorylation level in AS mice model, and the results showed that the protein phosphorylation level in the AS mice model was lower than that of the normal mice. The present study provides suitable fluorescence tool for further revealing phosphorylation related signaling pathways and disease mechanisms.

1. Introduction

Atherosclerosis (AS) is a chronic arterial disease, which is the main cause of coronary heart disease, cerebral infarction, peripheral vascular disease and other diseases [1–3]. At present, the universally recognized pathogenesis is the “endothelial injury response theory” [4,5], that is, the inflammatory and fibroproliferative response [6–9] of the artery to the damage of the intima of the artery caused by long-term dyslipidemia [10,11], hypertension [12], diabetes [13], smoking and other risk factors [2]. Oxidative stress mediated by active species and its subsequent chronic inflammation are recognized as the main initiating mechanism of the AS [14–16]. At present, the epigenetic effects of reactive oxygen

* Corresponding author.
E-mail address: zhangwei@sdnu.edu.cn (W. Zhang).

https://doi.org/10.1016/j.aca.2022.339825
Received 25 January 2022; Received in revised form 23 March 2022; Accepted 8 April 2022
Available online 20 April 2022

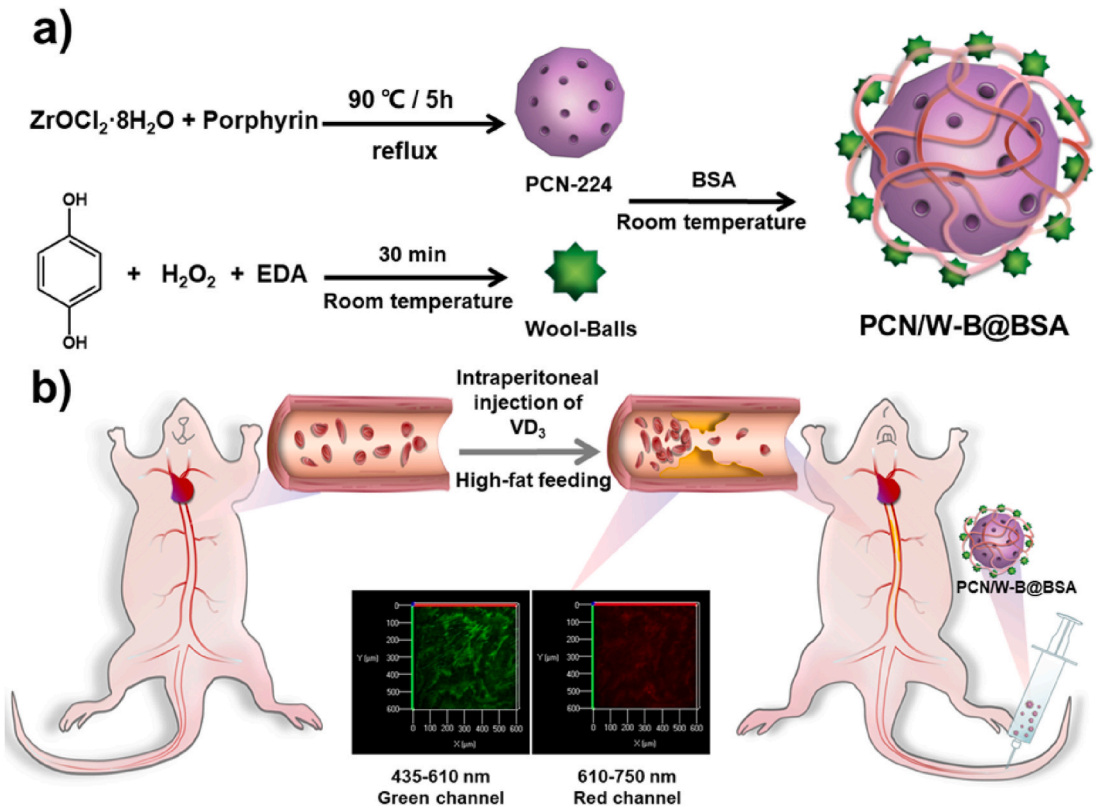

Scheme 1. Schematic diagram of preparation of fluorescent nanosensor and its application in monitoring phosphorylation level in atherosclerosis model.

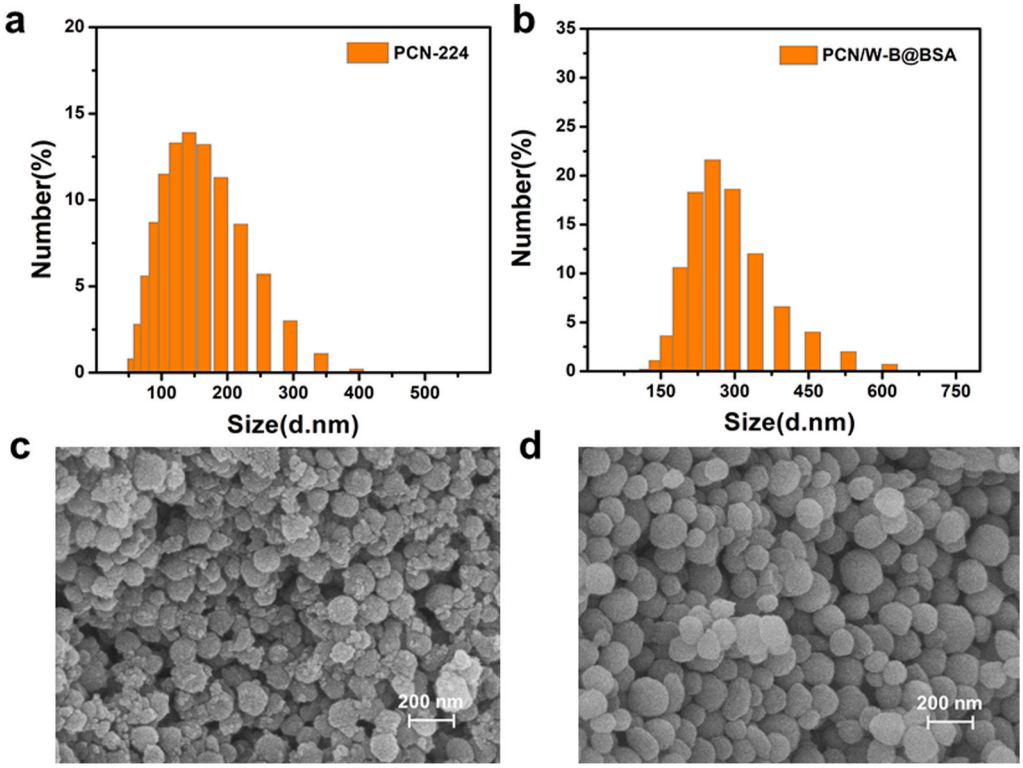

Fig. 1. Characterization of PCN-224 and PCN/W–B@BSA. (a) Hydrate particle size of PCN-224. (b) Hydrate particle size of PCN/W–B@BSA. (c) SEM images of PCN-224. (d) SEM images of PCN/W–B@BSA.

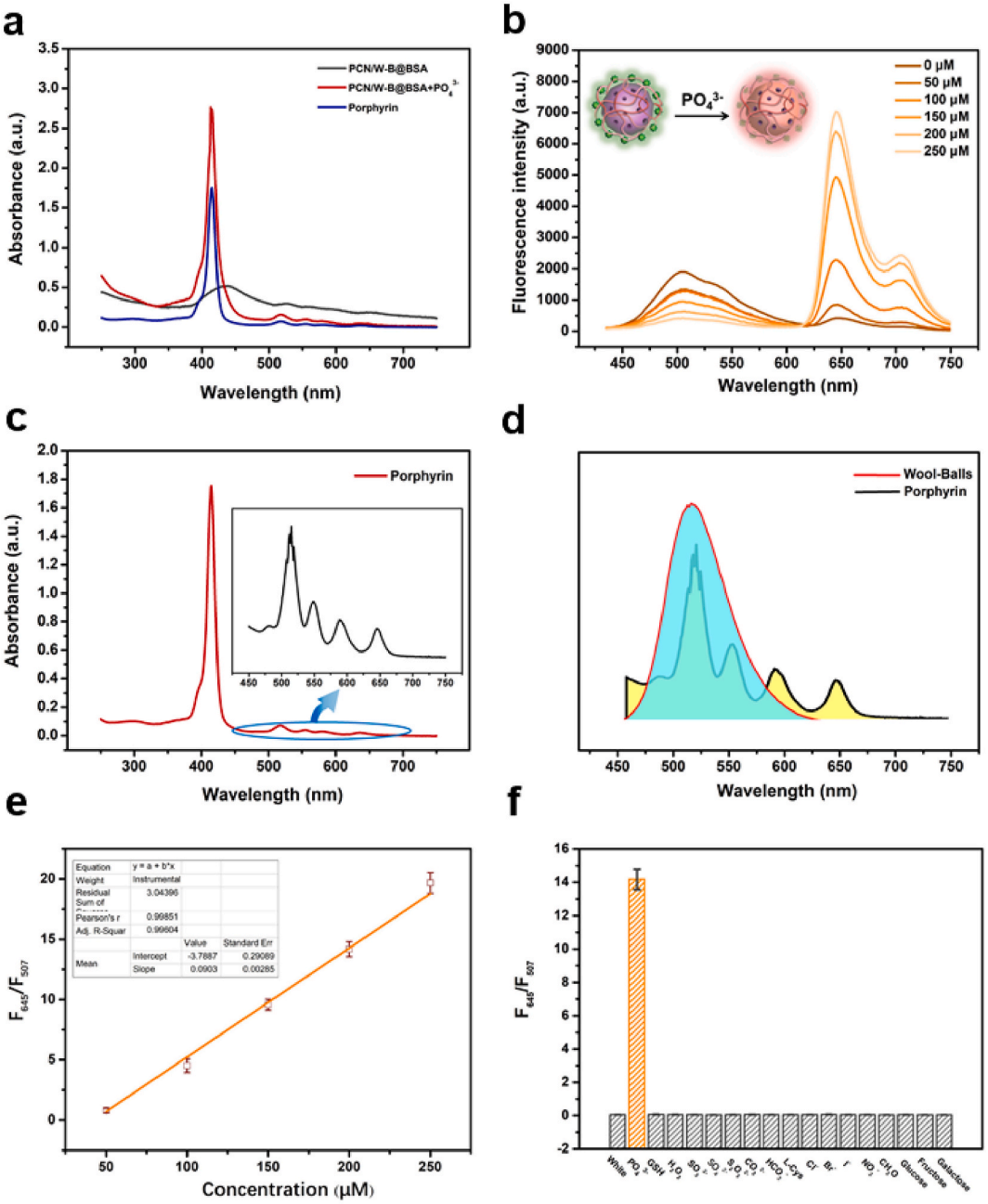

Fig. 2. (A) UV absorption of PCN-224 before and after incubation with phosphate. (b) Fluorescence spectra of PCN/W–B@BSA in response to different concentrations of phosphate; Experimental conditions: Ex = 415 nm, response time: 1.5h. (c) and (d) Spectral overlap between Wool-Balls and porphyrin molecules. (e) Operating curves, the ordinate is the ratio of the fluorescence intensity of the probe at 645 nm–507 nm, the linear range is 50–250 μM and the detection limit is 5.1 μM; Experimental conditions: Ex = 415 nm, response time: 1.5h. (f) Selective test of PCN/W–B@BSA, We selected the following concentrations for different substances: PO_4^{3-} (200 μM), GSH (1 mM), H_2O_2 (1 mM), SO_3^{2-} (1 mM), SO_4^{2-} (1 mM), $S_2O_3^{2-}$ (1 mM), CO_3^{2-} (1 mM), HCO_3^- (1 mM), L-Cys (200 μM), Cl^- (1 mM), Br^- (1 mM), I^- (1 mM), NO_3^- (1 mM), formaldehyde (50 μM), glucose (10 mM), fructose (10 mM), galactose (10 mM); Experimental conditions: Ex = 415 nm, response time: 1.5h.

species (ROS)-mediated oxidative modification on cells and tissues, including DNA methylation and protein post-translational modification, have not been elucidated. Therefore, the development of methods for probing protein post-translational modification levels in atherosclerotic diseases has important practical significance for studying the pathogenesis of AS.

Protein post-translational modification (PTMs), also known as covalent modification, is mainly to add functional groups with unique biochemical properties to proteins to change their functions through structural and property changes [17,18]. These modifications include phosphorylation [19], glycosylation [20,21], ubiquitination [22], nitrosylation [23], methylation [24], acetylation [25], lipidation [26], and proteolysis [27], and affect almost all aspects of normal cell biology and pathogenesis. Among them, protein phosphorylation is the most basic, universal and important mechanism to regulate and control protein activity and function. Evaluating protein phosphorylation level is an effective way to understand protein phosphorylation related signaling pathways of diseases, and it is of great significance to study the mechanism of diseases.

Currently, the methods of protein phosphorylation identification mainly include radioactive labeling, mass spectrometry, antibody labeling and enzymelinked immunoassay [28–31]. Biomass spectrometry

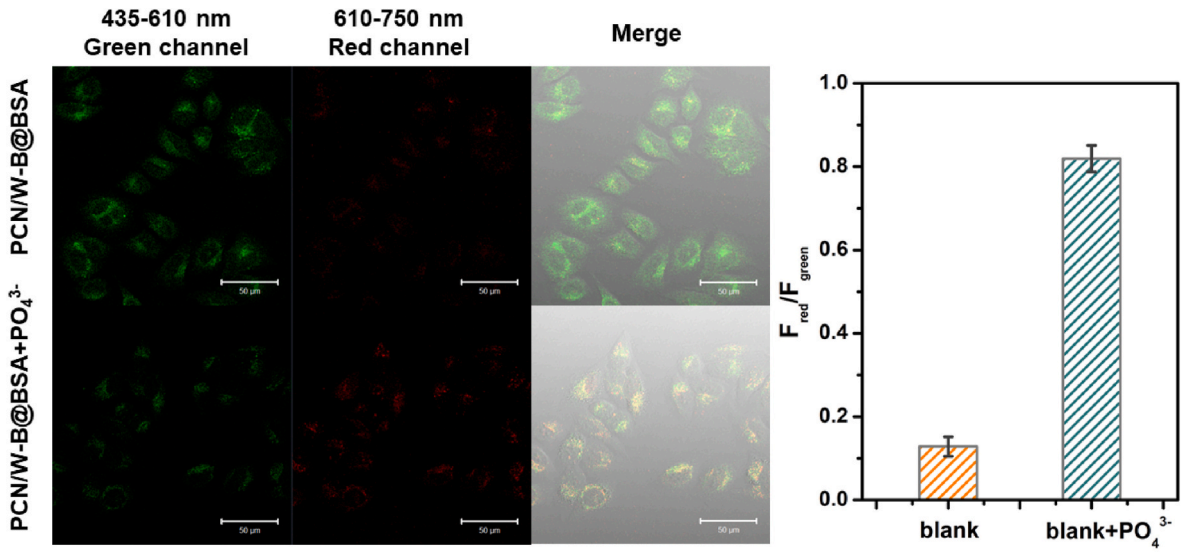

Fig. 3. Confocal fluorescence image of phosphorylation levels in SMCC-7721 cells and the output of fluorescence intensity, the intensity of the green channel decreased and the intensity of the red channel increased with the addition of phosphate; Experimental conditions: Ex = 415 nm, PO_4^{3-} (500 μM). (For interpretation of the references to color in this figure legend, the reader is referred to the Web version of this article.)

makes the study of protein phosphorylation easy [32], but the mass spectrometry requires the enzymatic hydrolysis of protein for mass spectrometry analysis, so as to realize real-time and *in situ* process analysis of protein post-translational modification site identification in biological systems, the mass spectrometry technology still has some difficulties. Fluorescence method is simple and feasible. Combined with imaging technology, real-time and *in situ* process analysis of phosphorylation level *in vivo* can be realized. Fluorescence probes have the characteristics of high sensitivity, low damage and good biocompatibility, providing an important tool for the detection of proteins post-translational modification levels and related pathophysiological studies. However, molecular fluorescent probes are still some problems such as short retention time, fast metabolism and easy diffusion when molecular probes are used for *in vivo* detection. Compared with traditional molecular probes, nanomaterials (such as quantum dots, carbon dots, metal nanomaterials, etc.) have many advantages such as high imaging sensitivity, long retention time *in vivo*, and simultaneous detection of multiple objects, which have attracted wide attention in the biomedical fields [33,34]. Therefore, development of new fluorescent probes based on nanomaterials is of great significance to reveal the mechanism of diseases.

Herein, the ratiometric fluorescent nanosensor for protein phosphorylation recognition was prepared using porphyrin molecules and fluorescent nanoclusters Wool-balls as fluorophore, respectively, and zirconium metal ions Zr(IV) of the PCN-224 as the active center, and thus the ratiometric fluorescence imaging of protein phosphorylation level in the AS mice model was realized. Specific recognition of phosphorylation sites is achieved *via* the selective interaction between the active center Zr(IV) and phosphate using fluorescence resonance energy transfer (FRET) mechanism. By using the two-photon properties of porphyrins, the background is significantly reduced, and thus the sensitivity of imaging is improved by combining with ratio imaging. The BSA was used to modify the surface of the nanosensor to reduce the nonspecific adsorption and thus improve the biocompatibility of the nanosensor. The AS model was established by one-time intraperitoneal injection of VD_3 combined with high-fat feeding, and the establishment of the model was proved by section staining and biochemical detection. Finally, the fluorescence nanosensor was successfully applied to fluorescence imaging of protein phosphorylation level in the AS mice model, and the experimental results showed that the protein phosphorylation level in the AS mice model was lower than that of the normal mice. This study provides a suitable fluorescence tool for further revealing phosphorylation related signaling pathways and disease mechanisms (Scheme 1).

2. Experimental

2.1. Materials, instrumentations and animals

2.1.1. Materials

$ZrOCl_2{\cdot}8H_2O$ (99.9%), Pyrrole (99%) were purchased from Macklin (Shanghai, China). Benzoic acid (99.5%) and 4-formylbenzoic acid (98%) were purchased from Aladdin Reagent Company (Beijing, China). Glutathione (97%) and L-cysteine (98%) were purchased from HEOWNS Reagent Company (Tianjin, China). Bovine serum (98.6%) protein was purchased from Sigma-Aldrich (Shanghai, China). N, N-dimethylformamide (99.5%), propionic acid (99.5%), dichloromethane (99.5%), hydroquinone (99.0–101.0%), hydrogen peroxide (30%), ethylenediamine (99.9%), K_3PO_4 (99.9%), Na_2SO_3 (97%), $NaSO_4$ (99%), $Na_2S_2O_3$ (99%), Na_2CO_3 (97%), $NaHCO_3$ (99.5%), NaCl (99.9%), KBr (99.5%), KI (99.0%), $NaNO_3$ (99.0%), formaldehyde (37.0–40.0%), glucose (99.9%), fructose (99.9%), and galactose (99.9%) were purchased from Sinopharm Chemical Reagent Co., Ltd. (Shanghai, China).

2.1.2. Instrumentations

Fluorescence Spectrometer (F-4700 HITACHT), ZHP-100 Constant temperature shaking incubator, UV–visible spectrophotometer (TU-1900), enzyme-labeled instrument (Synergy 2, Biotek, USA), DZF-6090 Vacuum drying oven, Zeta Potentiometer and DLS Dynamic light scatterometer (Malvern instruments Nano-ZS90), D8 ADVANCE X-ray powder diffractometer, Two-photon fluorescence microscope (Zeiss LSM 800 NLO), Electron microscope (HZTACHI HT7700), Analytical Balances (AR224CM), Eppendorf low-temperature high-speed centrifuge (Centrifuge 5430R).

2.1.3. Animals

The male Wistar mice (200 ± 10 g) and basic feed used in the experiment were purchased from Jinan Baosai Biotechnology Co., Ltd. All animal testing protocols are in accordance with the animal management regulations of the Ministry of Health of the People's Republic of China and have been approved by the Animal Care Committee of Shandong Normal University (Ethical committee approval number:

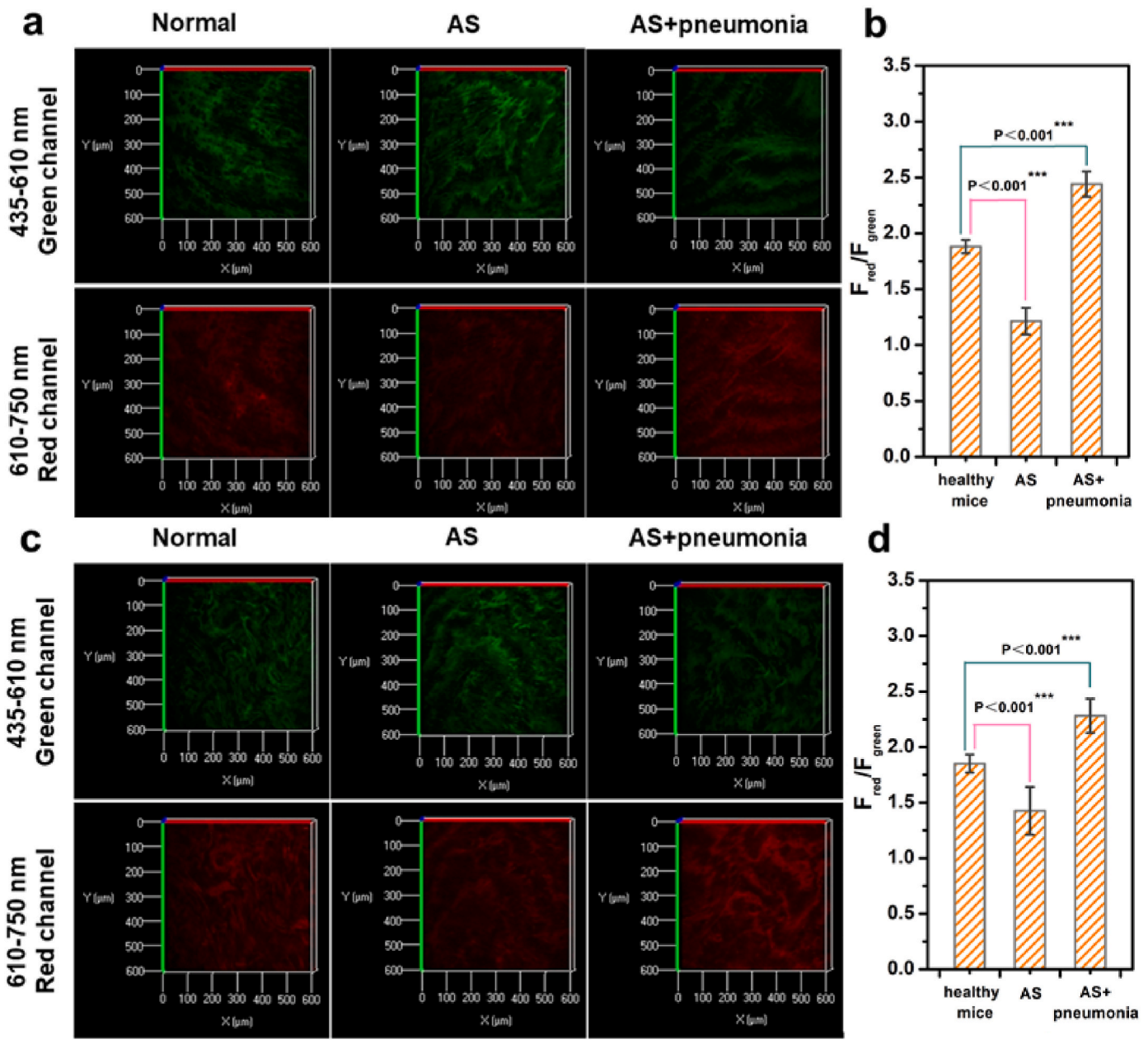

Fig. 4. (A) Two-photon fluorescence imaging of phosphorylation levels in mice thoracic aorta by PCN/W–B@BSA materials and (b) shows the output of fluorescence intensity. (c) Two-photon fluorescence imaging of phos-phorylation levels in mice abdominal aorta by PCN/W–B@BSA materials and (d) shows the output of fluorescence intensity. ***$p < 0.01$. Experimental conditions: Ex = 830 nm.

AEECSDNU2020041).

2.2. Synthetic procedures

2.2.1. Preparation of 5,10,15,20-tetra(4-carboxyphenyl)porphyrin

According to the reference [35], under the protection of N_2, added 400 mL redistilled propionic acid and 2.8 mL pyrrole into a 1000 mL three-necked round bottom flask, added 4-formylbenzoic acid (6 g, 0.04 mol), heated to 140 °C and reflux Stir for 1 h. After the reaction, it was reduced to room temperature and recrystallized at low temperature in dark place for 6 h to precipitate brown precipitation. Then suction filter the reaction solution and wash with dichloromethane until the crystal turns red brown and the washing solution is clear, and transfer the crystal to a vacuum drying oven to avoid light over night.

2.2.2. Preparation of wool-balls

Hydroquinone (400 mg) was dissolved in 7 mL deionized water, then 10 mL H_2O_2 (20%) was added to the solution, stired and added 3 mL ethylenediamine (EDA) to form nanoclusters within 30 min. Then the reaction solution was dialyzed overnight in 400 mL deionized water and cyclically steamed to obtain yellow-green wool-balls [36].

2.2.3. Preparation of PCN-224

According to the reference [37], dissolve $ZrOCl_2{\cdot}8H_2O$ (300 mg), porphyrin (100 mg) and benzoic acid (2.8 g) in 100 mL DMF at room temperature. Ultrasonic for 10 min to completely dissolve and heat to 90 °C, stir and reflux for 5 h. The purple precipitate was collected by centrifugation at 13 000 rpm, then washed with DMF and deionized water, and dispersed in deionized water for later use.

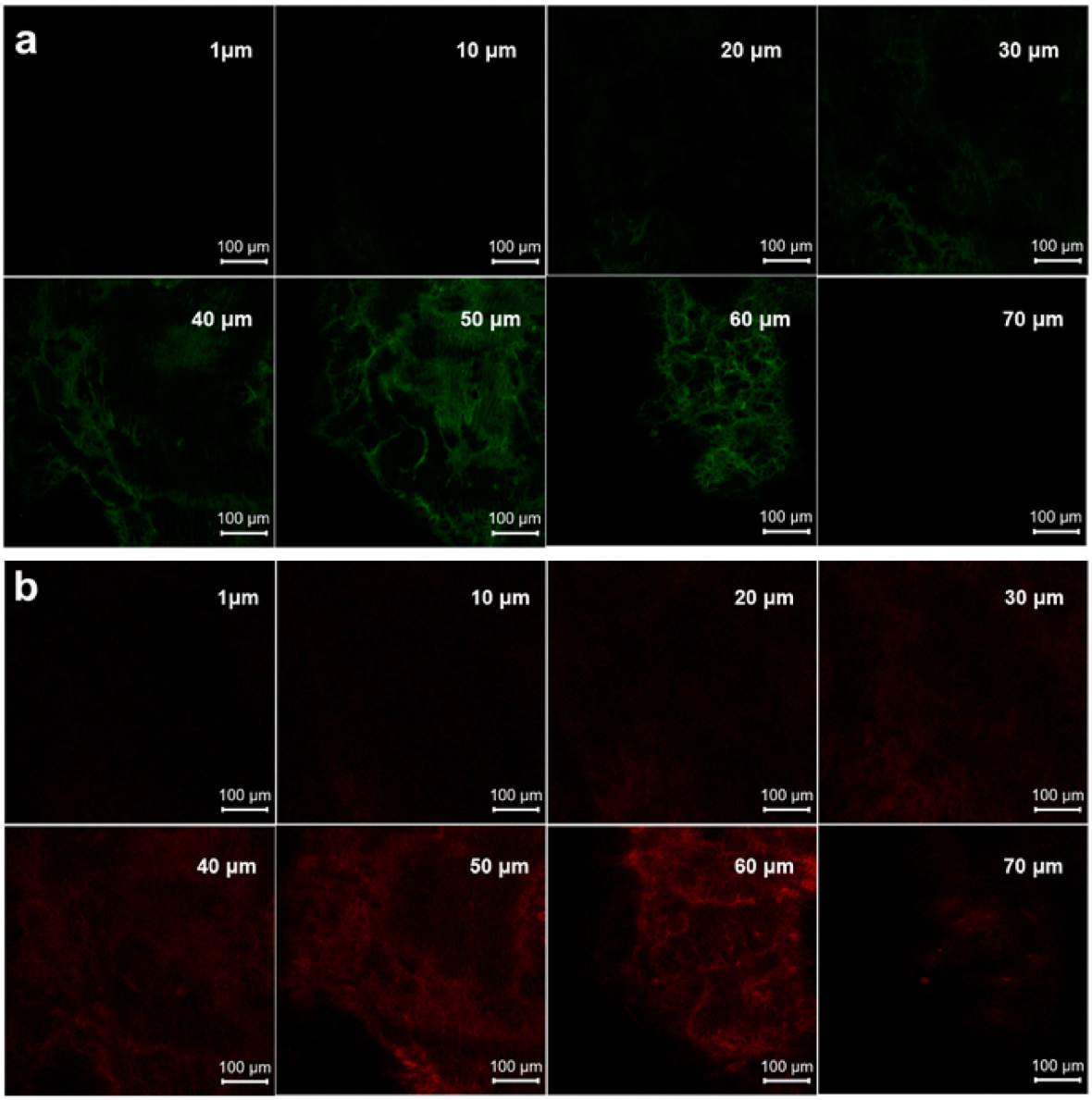

Fig. 5. Fluorescence imaging of phosphorylation levels using PCN/W–B@BSA at different depths in the inner wall of mice aorta under excitation of 830 nm, the emission range of (a) green channel was 435–610 nm, and that of (b) red channel was 610–750 nm. Experimental conditions: Ex = 830 nm. (For interpretation of the references to color in this figure legend, the reader is referred to the Web version of this article.)

2.2.4. Preparation of PCN/W–B@BSA

The Wool-Balls (400 mg) was added in 150 mL deionized water and used dilute hydrochloric acid to adjust the pH to 7, dispersed 100 mg PCN-224 into 50 mL deionized water and mixed it to the Wool-Balls solution, continue to stir for 10 min and heated to 30 °C. Then added 200 mg BSA to the mixed solution and stired at 30 °C for 30 min, the reaction solution was centrifuged at 8000 rpm and washed with deionized water until colorless, the reddish brown precipitate was dispersed in deionized water, and stored at low temperature.

2.2.5. Fluorescence quantum yield calculation

Quinine sulfate was selected as the standard substance to calculate the fluorescence quantum yield, and the calculation formula is as follows:

$$\varphi_1 = \frac{\varphi_B I_1 A_B \lambda_{exB} \eta_1}{I_B A_1 \lambda_{ex1} \eta_B}$$

The subscripts 1 and B refer to the sample and the reference material, respectively. φ: quantum yield; A: absorbance at the excitation wavelength; λex: the excitation wavelength; η: the refractive index of the solution; I: integrated area under the uncorrected emission spectra.

2.3. Cell experiment

2.3.1. Cell culture

SMCC-7721 cells were cultured in DMEM containing 1% antibiotics and 10% FBS and placed in a cell incubator containing 5% CO_2 at 37 °C.

2.3.2. Cell viability assay

SMCC-7721 cells were inoculated into a 96-well plate, placed at 37 °C, incubated overnight in a cell incubator containing 5% CO_2 for adherent growth, and then nanoparticles of 5, 10, 20, 30, 50, 75, 100, 200 and 300 mg/mL were successively added into the well plate for incubation for 12 h. The residual probe was cleaned with PBS, and then CCK-8 was added. After incubation for 1 h, the absorbance value at 450 nm was measured with a microplate reader.

2.3.3. Two-photon fluorescence imaging of cells

Before the experiment, the cells were inoculated into a dish a day earlier and allowed to stick to the wall. During imaging, the cells were first incubated with 30 μg/mL probe for 40 min to allow the probe to enter the cells, then cleaned with PBS to remove the residual probe and the cells were imaged in the PBS environment. After imaging, cells were incubated with phosphoric acid for 20 min, and imaging was continued after PBS cleaning.

2.4. Animal experiment

2.4.1. Establishment of animal models

According to the reference [38–40], male Wistar mice at 6–8 weeks were divided into three groups: blank group (n = 5), atherosclerosis group (n = 5) and pneumonia atherosclerosis group (n = 5). The blank group were fed with normal feed without restriction of water, and the AS group and the AS with pneumonia group were fed with high-fat feed for two months, namely 0.2% propyl thiouracil, 0.5% sodium cholate, 3% cholesterol, 5% white sugar, 10% lard and 81.3% basal feed. At the beginning of feeding, the AS group and the AS with pneumonia group were given a one-time intraperitoneal injection of vitamin D3 600 000 IU/kg, and the blank group was given intraperitoneal injection of the same volume of normal saline. Two months later, the AS group suffering from pneumonia were interfered with smoking, that is, the mice were inhaled with 10 cigarettes a day for a total of 10 days. After modeling, the lung tissues of healthy mice, AS mice and pneumonia + AS mice were taken for the detection of TNF-α by ELISA kit, and the main organs and aorta of different groups of mice were sectionized for staining, the tissue block below the coronal sulcus and 0.5 cm from the apex of the heart was sectioned for oil red O staining.

2.4.2. In vivo two-photon fluorescence imaging

The abdominal and thoracic cavity of mice were dissected longitudinally to expose the aorta. The root of coronary artery was taken to the lower iliac artery branch and the aorta was dissected longitudinally to expose the inner wall for imaging.

3. Results and discussion

3.1. Characterization of PCN/W–B@BSA

First, we synthesized the probe using Wool-Balls and PCN-224 as raw materials by room temperature stirring method, and carried out A series of characterization. The morphology and size of the materials were further characterized by dynamic light scattering (DLS), scanning electron microscope (SEM) and low power transmission electron microscopy (TEM). And the hydrated particle size of PCN-224 is about 140 nm, after doping Wool Balls with BSA coating, the hydrated particle size of the material increased to about 255 nm (Fig. 1a and b). SEM (Fig. 1c and d) and TEM (Fig. S1) indicated that the particle size of PCN-224 is about 90 nm and the particle size of the PCN/W–B@BSA is about 200 nm. The Zeta potential of PCN-224 before and after modification increased from −35.8 mV to −19.7 mV (Fig. S2), and IR spectra also confirmed that the fluorescent nanoprobe was successfully synthesized (Fig. S6). Meanwhile, PXRD of PCN-224, PCN/W–B@BSA, PCN/W–B@BSA (soaked in water for 5 days), PCN/W–B@BSA (stored at 60 °C for 10h), PCN/W–B@BSA (stored at −20 °C for 10 h) and PCN/W–B@BSA (stored under natural light for 16h) were scanned Image (Fig. S3), The results showed that the structure of the probe remained unchanged regardless of temperature, storage time or illumination. XPS analysis and surface element content determination of PCN-224 and PCN/W–B@BSA showed that S and N elements in the probe increased after doping Woo-balls and coating BSA (Figs. S4 and S5).

3.2. Fluorescence response and selectivity

Fluorescent nanoclusters were coated on the surface of PCN-224 under the action of BSA to form nanoprobe PCN/W–B@BSA. When the phosphate was not added, the probe emitted green fluorescence. And the phosphate coordinated with the zirconium metal node of PCN-224 after added, which interrupted the charge transfer (LMCT) between the ligand molecule and the metal, and the red fluorescence of porphyrin was restored. It is worth noting that the FRET occurred between them due to the overlap of absorption spectrum of porphyrin and emission spectrum of Wool-Balls, so that the fluorescence of porphyrin enhanced and the fluorescence of Wool-Balls weakened.

In order to study the optical properties of the probe, we explored the UV absorption properties of PCN/W–B@BSA that the PCN/W–B@BSA had obvious UV absorption at about 415 nm and the absorption strength increased significantly after the addition of phosphate (Fig. 2a). We further studied the fluorescence performance of the material by exciting the material with 415 nm excitation, and obtained the fluorescence spectra of PCN/W–B@BSA, with the addition of different concentrations of phosphate, the fluorescence of the material was quenched at 507 nm and strongly enhanced at 645 nm with the excitation wavelength of 415 nm (Fig. 2b). We believe that the addition of phosphate breaks the charge transfer between Zr(IV) and porphyrin in PCN-224 and restores the fluorescence of porphyrin molecules. This process was also confirmed by UV absorption spectrum, the absorption of porphyrin molecules is enhanced with the addition of phosphate (Fig. S7). In this process, the fluorescence change of the wool-balls is not affected by phosphate (Fig. S8). The fluorescence change of the Wool-Balls is due to the fluorescence emission spectrum of wool-balls at 450–625 nm overlapped with the absorption spectrum of porphyrin at this range (Fig. 2c and d, Fig. S9), so the FRET occurred between the two substances, which ultimately lead to fluorescence quenching of wool-balls and fluorescence enhancement of porphyrin. The fluorescence quantum yield of PCN-224 and Wool-Balls was also detected. The fluorescence quantum yield of Wool-Balls before and after the addition of PO_4^{3-} is 11.36% and 12.31%, the fluorescence quantum yield of PCN-224 before and after the addition of PO43- is 0.09% and 12.42%. We optimized the type of buffer solution, buffer concentration, buffer pH, probe concentration and response time to explore the optimal response environment for the probe (Fig. S10), and measured the linear fluorescence response of phosphate ions under the optimal conditions (Fig. 2e), the linear analysis shows that the linear response range of PCN/W–B@BSA to phosphate is 50–250 μM, the linear correlation coefficient is 0.9990, and has a detection limit of 5.1 μM.

We also tested the selectivity of the probe in the presence of various substances, and proved that the PCN/W–B@BSA has a good selectivity for phosphate in complex environment (Fig. 2f). At the same time, we gave the probe different reaction environment to test whether the probe is affected, such as changing the pH of buffer solution, or changing the viscosity of the reaction solution by changing the content of glycerol in the water, and the results showed that the probe is not affected by the pH and viscosity of the environment (Fig. S11). We also verified fluorescence response of the probe with other phosphorylated products under optimal conditions (Fig. S12), including phosphorylated amino acids, phosphorylated pep-tides, and phosphorylated proteins. It can be seen that the PCN/W–B@BSA can respond well to the above substances, so we believe that the PCN/W–B@BSA can be used to detect protein phosphorylation.

3.3. Application of nanoprobe in cells

We used the two-photon fluorescence microscope to explore the intracellular two-photon fluorescence imaging of PCN/W–B@BSA to demonstrate that the nanoprobe can be applied to fluorescence image of phosphorylation levels at the cellular level. We explored the two-photon properties of PCN/W–B@BSA (Fig. S13 and Fig. 3). The wavelength of

830 nm was used for excitation, and it was found that PCN/W–B@BSA had the maximum emission peak at 520 nm without the addition of phosphate. After addition of the phosphate, the fluorescence quenching of PCN/W–B@BSA at 520 nm is occurred, and the fluorescence at 640 nm is strongly enhanced, which consistent with the fluorescence properties of the nanoprobe. Therefore, we believe that PCN/W–B@BSA has good two-photon fluorescence properties. Before the cell experiment, CCK-8 was used to test the cytotoxicity of nanoparticles, and four kinds of nanoparticles were prepared for the cytotoxicity experiment. As shown in Fig. S14, the coating of BSA reduces the cytotoxicity of nanoparticles, and the PCN/W–B@BSA used in this study has the best biocompatibility. SMCC-7721 cells were incubated with the probe for 40 min, and then imaged with confocal microscopy. Bright green light and weak red light were observed inside the cells. After 500 μM PO_4^{3-} was added and incubated for 20 min, green fluorescence decreased and red fluorescence increased in cells. Therefore, we believe that PCN/W–B@BSA can detect intracellular phosphate.

3.4. Two-photon fluorescence imaging of the AS mice

Considering the probe has the excellent properties of selective recognition of phosphate in solution and in cells, we established AS mice model using the Wistar mice. And then pneumonia models induced by smoking based on AS mice model were established in order to demonstrate the versatility of the probe *in vivo*. H&E sections staining were performed on the aorta of different groups of mice to prove the establishment of the AS model (Fig. S15). H&E staining of lung sections in the three groups confirmed the formation of pneumonia model (Fig. S16). At the same time, we also proved the establishment of the mice model through other indicators (Figs. S17, S18, S19, S20). These results indicated that we have successfully established the AS mice model and pneumonia-AS model, respectively. At the same time, we tested the metabolism of the probe in mice after intravenous injection, and the results showed that PCN/W–B@BSA could be metabolized in about 36h in mice (Fig. S21).

To explore the differences in phosphorylation levels between healthy mice, the AS mice model, and the mice with pneumonia and the AS, we performed two-photon fluorescence imaging of the inner wall of the aorta in mice. Subsequently, three groups of mice were injected with the probe (10 mg/kg) through the tail vein. Compared with healthy mice, the intensity ratio of red channel to green channel (F_{red}/F_{green}) in the thoracic aorta of atherosclerotic mice was decreased, suggesting that the phosphorylation level of atherosclerotic thoracic aorta of mice was lower than that of normal mice. In mice with AS pneumonia, the intensity ratio of red channel to green channel increased, indicating that phosphorylation levels in mice with AS pneumonia were higher than those in normal mice (Fig. 4a and b). The results of abdominal aorta experiment were consistent with the above results (Fig. 4c and d).

We also made two-photon probes to image the inner wall of the aorta in mice at different depths. Under excitation at 830 nm, the probe imaged the inner wall of the vessel at depths of 1 μm, 10 μm, 20 μm, 30 μm, 40 μm, 50 μm, 60 μm, and 70 μm, as shown in Fig. 5, the emission range of green channel was 435–610 nm, and that of red channel was 610–750 nm. These results indicate that the nanoprobes are suitable for detecting phosphorylation levels and two-photon imaging in mice models of AS.

4. Conclusions

In this work, the ratiometric fluorescent nanosensor was prepared using Zr(IV) as the recognition site, and the porphyrins and the woolballs as fluorophores, respectively, which achieved ratio imaging analysis of phosphorylation level and revealed protein phosphorylation level in the AS model. Employing two-photon fluorescence imaging, the background is significantly reduced, and combined with ratio imaging, the sensitivity of imaging analysis is improved. The BSA was used to modify the surface of the nanosensor to reduce the nonspecific adsorption and improve the biocompatibility of the nanosensor. The model of AS was established and confirmed by section staining and inflammatory factor test. Finally, the fluorescence nanosensor was successfully applied to fluorescence imaging of protein phosphorylation level in the AS model, and the experimental results showed that the protein phosphorylation level in the AS model was lower than that of the normal mice. The present study provides a good fluorescence tool for further revealing phosphorylation related signaling pathways and disease mechanisms.

CRediT authorship contribution statement

Wei Zhang: Supervision, Methodology, Validation, Data curation, Formal analysis, Writing – original draft, Funding acquisition, Conceptualization, Writing – review & editing. **Jin Li:** Methodology, Validation, Data curation, Formal analysis, Writing – original draft. **Na Zhao:** Methodology, Validation, Data curation, Formal analysis, Writing – original draft. **Ping Li:** Data curation, Validation. **Wen Zhang:** Investigation, Data curation. **Hui Wang:** Methodology, Resources. **Bo Tang:** Funding acquisition, Conceptualization, Writing – review & editing.

Declaration of competing interest

The authors declare that they have no known competing financial interests or personal relationships that could have appeared to influence the work reported in this paper.

Acknowledgment

This work was supported by National Key R&D Program of China (2019YFA0210100), National Natural Science Foundation of China (21927811, 22076106 and 21874084), Natural Science Foundation of Shandong Province (ZR2019JQ07), and the Key Research and Development Program of Shandong Province (2018YFJH0502).

Appendix A. Supplementary data

Supplementary data to this article can be found online at https://doi.org/10.1016/j.aca.2022.339825.

References

[1] J. Frostegård, Immunity, Atherosclerosis and cardio-vascular disease, BMC Med. 11 (2013) 117, https://doi.org/10.1186/1741-7015-11-117.
[2] P. Libby, The changing landscape of atherosclerosis, Nature 592 (2021) 524–533, https://doi.org/10.1038/s41586-021-03392-8.
[3] A.J. Lusis, Atherosclerosis, Nature 407 (2000) 233–241, https://doi.org/10.1038/35025203.
[4] P.M. Ridker, B.M. Everett, T. Thuren, J.G. MacFadyen, W.H. Chang, C. Ballantyne, F. Fonseca, J. Nicolau, W. Koenig, S.D. Anker, J.J.P. Kastelein, Cornel, J.H.P. Pais, D. Pella, J. Genest, R. Cifkova, A. Lorenzatti, T. Forster, Z. Kobalava, L. Vida-Simiti, et al., Antiinflammatory therapy with canakinumab for atherosclerotic disease, N. Engl. J. Med. 377 (2017) 1119–1131, https://doi.org/10.1056/NEJMoa1707914.
[5] P. Libby, G.K. Hansson, From focal lipid storage to systemic inflammation: JACC review topic of the week, J. Am. Coll. Cardiol. 74 (2019) 1594–1607, https://doi.org/10.1016/j.jacc.2019.07.061.
[6] K.J. Moore, F.J. Sheedy, E.A. Fisher, Macrophag-es in atherosclerosis: a dynamic balance, Nat. Rev. Immunol. 13 (2013) 709–721, https://doi.org/10.1016/j.jacc.2019.07.061.
[7] O. Soehnlein, P. Libby, Targeting inflammation in atherosclerosis — from experimental insights to the clinic, Nat. Rev. Drug Discov. 20 (2021) 589–610, https://doi.org/10.1038/s41573-021-00198-1.
[8] I. Tabas, A.H. Lichtman, Monocyte-Macrophages and T Cells in atherosclerosis, Immunity 47 (2017) 621–634, https://doi.org/10.1016/j.immuni.2017.09.008.
[9] H.L. Teague, A.M. Ahlman, A. Alavi, D.D. Wagner, A.H. Lichtman, M. Nahrendorf, F.K. Swirski, F. Nestle, J.M. Gelfand, M.J. Kaplan, S. Grinspoon, P.M. Ridker, D. E. Newby, A. Tawakol, Z.A. Fayad, N.N. Mehta, Unraveling vascular inflammation: from immu-nology to imaging, J. Am. Coll. Cardiol. 70 (2017) 1403–1412, https://doi.org/10.1016/j.jacc.2017.07.750.

[10] U. Laufs, K.G. Parhofer, H.N. Ginsberg, R.A. Hegele, Clinical review on triglycerides, Eur. Heart. 41 (2020) 99–109c, https://doi.org/10.1093/eurheartj/ehz785.
[11] S. Raposeiras-Roubin, X. Rosselló, B. Oliva, L. Fernández-Friera, L.M. Mendiguren, V. Andrés, H. Bueno, J. Sanz, V. Martínez de Vega, E. Abu-Assi, A. Iñiguez, A. Fernández-Ortiz, B. Ibáñez, V. Fuster, Triglycerides and residual atherosclerotic risk, J. Am. Coll. Cardiol. 77 (2021) 3031–3041, https://doi.org/10.1016/j.jacc.2021.04.059.
[12] L. Fernández-Friera, V. Fuster, B. López-Melgar, B. Oliva, J. Sánchez-González, A. Macías, B. Pérez-Asenjo, D. Zamudio, J.C. Alonso-Farto, S. España, J. Mendiguren, H. Bueno, J.M. García-Ruiz, B. Ibañez, A. Fernández-Ortiz, J. Sanz, Vascular inflammation in subclinical atherosclerosis detected by hybrid PET/MRI, J. Am. Coll. Cardiol. 73 (2019) 1371–1382, https://doi.org/10.1016/j.jacc.2018.12.075.
[13] R.H. Eckel, K.E. Bornfeldt, I. Goldberg, Cardio-vascular disease in diabetes, beyond glucose, J. Cell. Metab. 33 (2021) 1519–1545, https://doi.org/10.1016/j.cmet.2021.07.001.
[14] S.J. Forrester, D.S. Kikuchi, M.S. Hernandes, Q.S. Xu, K.K. Griendling, Reactive oxygen species in metabolic and inflammatory signaling, Circ. Res. 122 (2018) 877–902, https://doi.org/10.1161/circresaha.117.311401.
[15] U. Förstermann, N. Xia, H. Li, Roles of vascular oxidative stress and nitric oxide in the pathogenesis of atherosclerosis, Circ. Res. 120 (2017) 713–735, https://doi.org/10.1161/circresaha.116.309326.
[16] E. Schleicher, U. Friess, Oxidative stress, AGE, and atherosclerosis, Kidney, Bar Int. 72 (2007) S17–S26, https://doi.org/10.1038/sj.ki.5002382.
[17] E.K. Keenan, D.K. Zachman, M.D. Hirschey, Dis-covering the landscape of protein modifications, Mol. Cell. 81 (2021) 1868–1878, https://doi.org/10.1016/j.molcel.2021.03.015.
[18] M. Mann, O.N. Jensen, Proteomic analysis of post-translational modifications, Nat. Biotechnol. 21 (2003) 255–261, https://doi.org/10.1038/nbt0303-255.
[19] J.A. Ubersax, J.E. Ferrell Jr., Mechanisms of specificity in protein phosphorylation, Nat. Rev. Mol. Cell Biol. 8 (2007) 530–541, https://doi.org/10.1038/nrm2203.
[20] J. Eichler, Protein glycosylation, Curr. Biol. 29 (2019) R229–R231, https://doi.org/10.1016/j.cub.2019.01.003.
[21] K.T. Schjoldager, Y. Narimatsu, H.J. Joshi, H. Clausen, Global view of human protein glycosylation pathways and functions, Nat. Rev. Mol. Cell Biol. 21 (2020) 729–749, https://doi.org/10.1038/s41580-020-00294-x.
[22] N. Foot, T. Henshall, S. Kumar, Ubiquitination and the regulation of membrane proteins, Physiol. Rev. 97 (2016) 253–281, https://doi.org/10.1152/physrev.00012.2016.
[23] J.S. Stamler, S. Lamas, F.C. Fang, Nitrosylation: the prototypic redox-based signaling mechanism, Cell 106 (2001) 675–683, https://doi.org/10.1016/s0092-8674(01)00495-0.
[24] J. Murn, Y. Shi, The winding path of protein meth-ylation research: milestones and new frontiers, Nat. Rev. Mol. Cell Biol. 18 (2017) 517–527, https://doi.org/10.1038/nrm.2017.35.
[25] K.J. Menzies, H. Zhang, E. Katsyuba, J. Auwerx, Protein acetylation in metabolism — metabolites and cofactors, Nat. Rev. Endocrinol. 12 (2016) 43–60, https://doi.org/10.1038/nrendo.2015.181.
[26] H. Jiang, X. Zhang, X. Chen, P. Aramsangtienchai, Z. Tong, H. Lin, Protein lipidation: occurrence, mecha-nisms, biological functions, and enabling technologies, Chem. Rev. 118 (2018) 919–988, https://doi.org/10.1021/acs.chemrev.6b00750.
[27] N. Chondrogianni, I. Petropoulos, S. Grimm, K. Georgila, B. Catal-gol, B. Friguet, T. Grune, E.S. Gonos, Protein damage, repair and proteolysis, Mol. Aspect. Med. 35 (2014) 1–71, https://doi.org/10.1016/j.mam.2012.09.001.
[28] F.M. White, A. Wolf-Yadlin, Methods for the analysis of protein phosphorylation–mediated cellular signaling networks, Annu. Rev. Anal. Chem. 9 (2016) 295–315, https://doi.org/10.1146/annurev-anchem-071015-041542.
[29] J. Ptacek, M. Snyder, Charging it up: global analysis of protein phosphorylation, Trends Genet. 22 (2006) 545–554, https://doi.org/10.1016/j.tig.2006.08.005.
[30] D. Bonenfant, T. Schmelzle, E. Jacinto, L. Crespo José, T. Mini, N. Hall Michael, P. Jenoe, Quantitation of changes in protein phosphorylation: a simple method based on stable isotope labeling and mass spectrometry, P. Natl. Acad. Sci. 100 (2003) 880–885, https://doi.org/10.1073/pnas.232735599.
[31] S. Torii, H. Yamaguchi, A. Nakanishi, S. Arakawa, S. Honda, K. Moriwaki, H. Nakano, S. Shimizu, Identification of a phosphorylation site on Ulk1 required for genotoxic stress-induced alternative autophagy, Nat. Commun. 11 (2020) 1754, https://doi.org/10.1038/s41467-020-15577-2.
[32] R. Aebersold, M. Mann, Mass-spectrometric explora-tion of proteome structure and function, Nature 537 (2016) 347–355, https://doi.org/10.1038/nature19949.
[33] N.P. Damayanti, L.L. Parker, J.M.K. Irudayaraj, Fluorescence lifetime imaging of biosensor peptide phos-phorylation in single live cells, angew, Chem. Int. Ed. 52 (2013) 3931–3934, https://doi.org/10.1002/anie.201209303.
[34] Y. Yang, Q. Zhao, W. Feng, F. Li, Luminescent chemodosimeters for bioimaging, Chem. Rev. 113 (2013) 192–270, https://doi.org/10.1021/cr2004103.
[35] W. Zhang, J. Xu, P. Li, X. Gao, W. Zhang, H. Wang, B. Tang, Treatment of hyperphosphatemia based on specific interactions between phosphorus and Zr(iv) active centers of nano-MOFs, Chem. Sci. 9 (2018) 7483–7487, https://doi.org/10.1039/c8sc02638f.
[36] B.-B. Chen, X.-Y. Wang, R.-C. Qian, Rolling “wool-balls”: rapid live-cell mapping of membrane sial-ic acids via poly-p-benzoquinone/ethylenediamine nanoclusters, Chem. Commun. 55 (2019) 9681–9684, https://doi.org/10.1039/c9cc03338f.
[37] J. Park, Q. Jiang, D. Feng, L. Mao, H.-C. Zhou, Size-controlled synthesis of porphyrinic metal–organic framework and functionalization for targeted photodynamic therapy, J. Am. Chem. Soc. 138 (2016) 3518–3525, https://doi.org/10.1021/jacs.6b00007.
[38] N. Lian, J. Tong, W. Li, J. Wu, Y. Li, Ginkgetin ameliorates experimental atherosclerosis in rats, Biomed. Pharmacother. 102 (2018) 510–516, https://doi.org/10.1016/j.biopha.2018.03.107.
[39] P. Shi, H. Ji, H. Zhang, J. Yang, R. Guo, J. Wang, circANRIL reduces vascular endothelial injury, oxida-tive stress and inflammation in rats with coronary atherosclerosis, Exp. Ther. Med. 20 (2020) 2245–2251, https://doi.org/10.3892/etm.2020.8956.
[40] J. Kearley, Jonathan S. Silver, C. Sanden, Z. Liu, Aaron A. Berlin, N. White, M. Mori, T.-H. Pham, Christine K. Ward, Gerard J. Criner, N. Marchetti, T. Mustelin, Jonas S. Erjefalt, R. Kolbeck, Alison A. Humbles, Humbles, A. Alison, Cigarette smoke silences innate lymphoid cell function and facilitates an exacerbated type I interleu-kin-33-dependent response to infection, Immunity 42 (2015) 566–579, https://doi.org/10.1016/j.immuni.2015.02.011.